Unique dislocation loops distribution of AlCrFeNiTi$_x$ eutectic high-entropy alloys under high-temperature ion irradiation

Yibo Wang [a,1], Songyuan Li [a,1], Feida Chen [a,*], Kun Yang [a], Guojia Ge [a], Xiaobin Tang [a,b], Minyu Fan [c], Ping Huang [c]

[a] Department of Nuclear Science & Technology, Nanjing University of Aeronautics and Astronautics, Nanjing 211106, China
[b] Key Laboratory of Nuclear Technology Application and Radiation Protection in Astronautics, Ministry of Industry and Information Technology, Nanjing 211106, China
[c] Suzhou Nuclear Power Research Institute, Suzhou 215004, China

ARTICLE INFO

ABSTRACT

Eutectic high-entropy alloys (EHEAs) have drawn great attention due to their excellent high-temperature mechanical properties. A group of EHEAs AlCrFeNiTi$_x$ with different titanium contents was irradiated with 3 MeV Fe^{11+} ions at 500 °C with fluences of 9.1×10^{14} and 4.55×10^{15} ions/cm^2. The disordered body-centered-cubic (BCC, A2) exhibited smaller-sized dislocation loops than those of ordered BCC (B2) based on Transmission electron microscopy (TEM) analysis. The type of loops found in AlCrFeNi alloy were < 100 > and 1/2 < 111 >. The fraction of 1/2 < 111 > was higher, indicating the excellent irradiation resistance of EHEAs. Small size and large density of dislocation loops formed after the addition of Ti. Phase boundaries in the alloys could effectively decrease the density and size of dislocation loops because of defects annihilation at phase boundaries. In combination with density function theory (DFT) results. B2 phase exhibited better energy landscape advantage in the Ti accommodating, and the MSD results indicated that the lattice distortion effect caused by Ti entering B2 phase was more obvious than A2 according to the density function theory (DFT) results. Our research exhibited a beneficial scheme for solid solution strengthening of elements in EHEAs, and provided an insight into the suppression of dislocation loops under irradiation.

© 2023 Elsevier B.V. All rights reserved.

1. Introduction

High-entropy alloys (HEAs), which are composed of four or more principal elements in equal-molar or near equal-molar fraction, have promising potential in advanced nuclear systems [1,2]. Compared to single-phase HEAs, eutectic HEAs (EHEAs) have attracted broad attention high-temperature applications due to their dual-phase structures, stable defect structures, and good creep resistance [3–5]. Moreover, the microstructures of dense lamellar microstructures and a mass of phase boundaries can be formed in EHEAs, which act sinks for defect (e.g., vacancies and interstitials atoms), demonstrating the significant advantage in materials for nuclear application especially for improving radiation resistance [6,7].

However, the in-pile application of EHEAs is recognized to be vulnerable to high flux of neutrons, which results in remarkably radiation damages such as irradiation hardening and swelling, significantly reducing its mechanical properties [8,9]. Therefore, a clear distinguishment of dislocation loop types is essential for understanding the mechanism of materials for failures due to irradiation hardening and embrittlement. For example, despite the fact that < 100 > and 1/2 < 111 > dislocation loops both existed in body-centered-cubic (BCC) steels. The research found that < 100 > dislocation loops have low mobility, and may cause sclerosis by impeding the movement of dislocation loops, while 1/2 < 111 > dislocation loops were glissile relatively [10]. Although extensive studies on the mechanical properties of EHEAs have been performed, there is lacking of necessary information about the distribution of radiation-induced dislocation loops in EHEAs, which is very critical for a fundamental understanding of the behavior of radiation defects and the potential applications of EHEAs in the nuclear system. Al-Co-Cr-Fe-Ni was a widely known material in EHEAs due to its excellent strength and ductility [11] which showed good mechanical properties. However, the element Co in the alloy system has high neutron transmutation-induced radioactivity, which prohibited its application in nuclear

---

energy systems. Composition optimization design is an effective way to enhance the microstructure and mechanical properties of the alloy. A large number of studies have focused on adding micro-alloying elements. It was suggested that replacement of Ti with Co results in superior properties such as low density, high melting point, large atomic radius and reduced activity based on the micro-element regulation, which was previously recognized as an effective method to enhance it performance in nuclear system [12–15]. Thus, it is worth enhance its performance in nuclear system.

In the present work, EHEAs AlCrFeNiTi$_x$ with different Ti ratio was chosen as a prototype to study the distribution of the dislocation loops of EHEAs. The samples were irradiated by 3 MeV Fe ions with the fluence of 9.1×10^{14} and 4.55×10^{15} ions/cm^2 at 500 °C. Irradiation-induced defects were characterized by transmission electron microscopy (TEM), followed by quantifying the size, density, and type of dislocation loops of EHEAs were quantified. Moreover, density function theory (DFT) calculations were conducted to clarify the mechanism of dislocation loops distribution.

2. Experimental

2.1. Materials synthesis and ion irradiation

AlCrFeNiTi$_x$ (x = 0, 0.5, 1) alloys were prepared by cold crucible levitation melting under argon atmosphere, and denoted as "Ti0", "Ti0.5" and "Ti1". The purity of raw ingots is higher than 99.95 % as characterized by ICP-MS as shown in previous publish [14], The ingots were rolled and remelted at least four times to ensure the chemical homogeneity.

The irradiation experiments were performed on the 320 kV platform at the Institute of Modern Physics, Chinese Academy of Sciences. The EHEAs were irradiated with 3 MeV Fe^{11+} ions to fluences of 9.1×10^{14} and 4.55×10^{15} ions/cm^2 at 500 °C with vacuum of 1×10^{-6} Pa. Stopping and Range of Ions in Matter (SRIM) 2013 code in "TRIM" mode was used to estimate the displacement per atom (dpa) and Fe concentration. Threshold displacement energy of aluminum, titanium and other elements were determined as 25 eV, 30 eV and 40 eV, respectively [16,17]. The density of 6.63 g/cm^3, 6.41 g/cm^3 and 6.22 g/cm^3 was experimentally determined for Ti0, Ti0.5 and Ti1 via Archimedes method with a balance, respectively, and used in SRIM simulation. The SRIM calculation results of dpa and Fe distribution are summarized in Fig. 1 in the Supplementary material, and the peak damages for Ti0 are approximately 1.4 and 7 dpa, respectively.

2.2. Microstructural characterization

The TEM sample of Ti0 irradiated at 1.4 dpa was prepared by mechanical polishing to about 60 μm thickness, followed by twin-jet electropolishing (MTP-1A) in ethanol solution containing 9 % HClO$_4$. The other TEM samples were prepared by focused ion beam equipped on a Helios 5 UX, followed by "flash polishing" to remove the FIB-induced damages. The final thickness of TEM foils is about 70 nm.

The irradiation-induced defects were characterized by TEM and STEM (FEI Talos F200X operated at 200 kV with two-beam conditions) both in bright-field (BF) and dark-field (DF). The size and density of dislocation loops were calculated in the software of Nano-measurement. In order to reduce deviation for each sample, the size and number densities data of dislocation loops were calculated by taking average at least five TEM images.

2.3. Simulation methodology

DFT was employed to further explore the fundamental mechanism and propose a reliable theoretical explanation from the

microscopic perspective. A framework of A2/B2 was obtained from Material Studio, and the model containing 64 atoms of BCC lattices were utilized for the atomistic calculations with Vienna *Ab-initio* Simulation Package code [18,19]. The generalized gradient approximation (GGA) with Perdew-Burke-Emzerhot (PBE) functional was used as exchange-correlation. Plane wave cutoffs 500 and 330 eV were used to calculate the A2 and B2 phase, respectively. The irreducible Brillouin Zone was sample with $2 \times 2 \times 3$ k-point meshes for all calculations. The relaxation of electronic was achieved until the change of the total energy was smaller than 10^{-6} eV/cell. The geometries of A2/B2 system are optimized with the force until the maximum forces on the ions were smaller than 0.01 eV/Å. The ab-initio molecular dynamics (AIMD) was operated at 770 K under NVT ensemble, and whole system relaxed for 1 *ps*. The results of radial distribution function (RDF) and mean square displacement (MSD) are processed by *OVITO* software and *VASPKIT* code respectively [20].

3. Results

3.1. Types of dislocation loops in AlCrFeNi

The dislocation loops in materials should be characterized and differentiated in order to understanding the different contributions of dislocation loops to radiation hardening. The density of both types of dislocation loops was quantified based on the methodology proposed by Yao [21].

Table 1 presents the **g·b** value and crystallographic information between dislocation-loop habit planes and (002) planes imaged under the [001] zone axis. Based on the information summarized in Table 1, a dislocation loop morphology map at on-zone condition was constructed, as is shown in Fig. 1(b) with the corresponding diffraction pattern for the zone axis of [001]. In terms of the alignments and shapes of dislocation loops, it is easy to distinguish the types. Fig. 1(c-d) presents STEM images formed using $\mathbf{g}_{0\bar{2}0}$ and $\mathbf{g}_{110}$ diffraction vectors near the zone axis, which clearly indicate 1/2(111) and 1/2(11$\bar{1}$) loops, respectively. Some edge-on dislocation loops marked with blue arrows were observed parallel to the [020] direction, as shown in Fig. 1(d), but invisible in Fig. 1(c). These dislocation loops are (100) type according to the dislocation–loop map in Fig. 1(b).

As discussed, some dislocation loops are invisible when the **g** vectors satisfy the invisibility condition of **g·b** = 0. Therefore, only 2/3 of the density of < 100 > dislocation loops and half of the density of 1/2 < 111 > dislocation loops can be observed when **g** = (110). Moreover, only 1/3 of the density of < 100 > dislocation loops and all the density of 1/2 < 111 > dislocation loops can be observed when **g** = (0$\bar{2}$0), as expressed in Eqs. (1) and (2). Based on the densities counted using the diffraction condition with different **g** vectors, the accurate density of < 100 > dislocation loops and 1/2 < 111 > dislocation loops can be obtained using Eqs. (3) and (4) [21].

$$\rho_{g=(110)} = 2/3\rho_{b=<100>} + 1/2\rho_{b=1/2<111>} \tag{1}$$

$$\rho_{g=(0\bar{2}0)} = 1/3\rho_{b=<100>} + \rho_{b=1/2<111>} \tag{2}$$

$$\rho_{b=<100>} = 2\rho_{g=(110)} - \rho_{g=(0\bar{2}0)} \tag{3}$$

$$\rho_{b=1/2<111>} = -2/3\rho_{g=(110)} + 2\rho_{g=(0\bar{2}0)} \tag{4}$$

where $\rho_{g=(110)}$ and $\rho_{g=(0\bar{2}0)}$ are the densities of dislocation loops observed using **g** vector of (110) and (0$\bar{2}$0), and $\rho_{b<100>}$ and $\rho_{b=1/2<111>}$ are the densities of < 100 > and < 111 > dislocation loops, respectively.

The number densities of < 100 > and 1/2 < 111 > dislocation loops for A2 phase are 1.10×10^{21} and 1.95×10^{21} /m^3, respectively. Similarly, the number densities of < 100 > and 1/2 < 111 > dislocation loops for B2 phase are 3.42×10^{20} and 3.02×10^{21} /m^3, respectively.
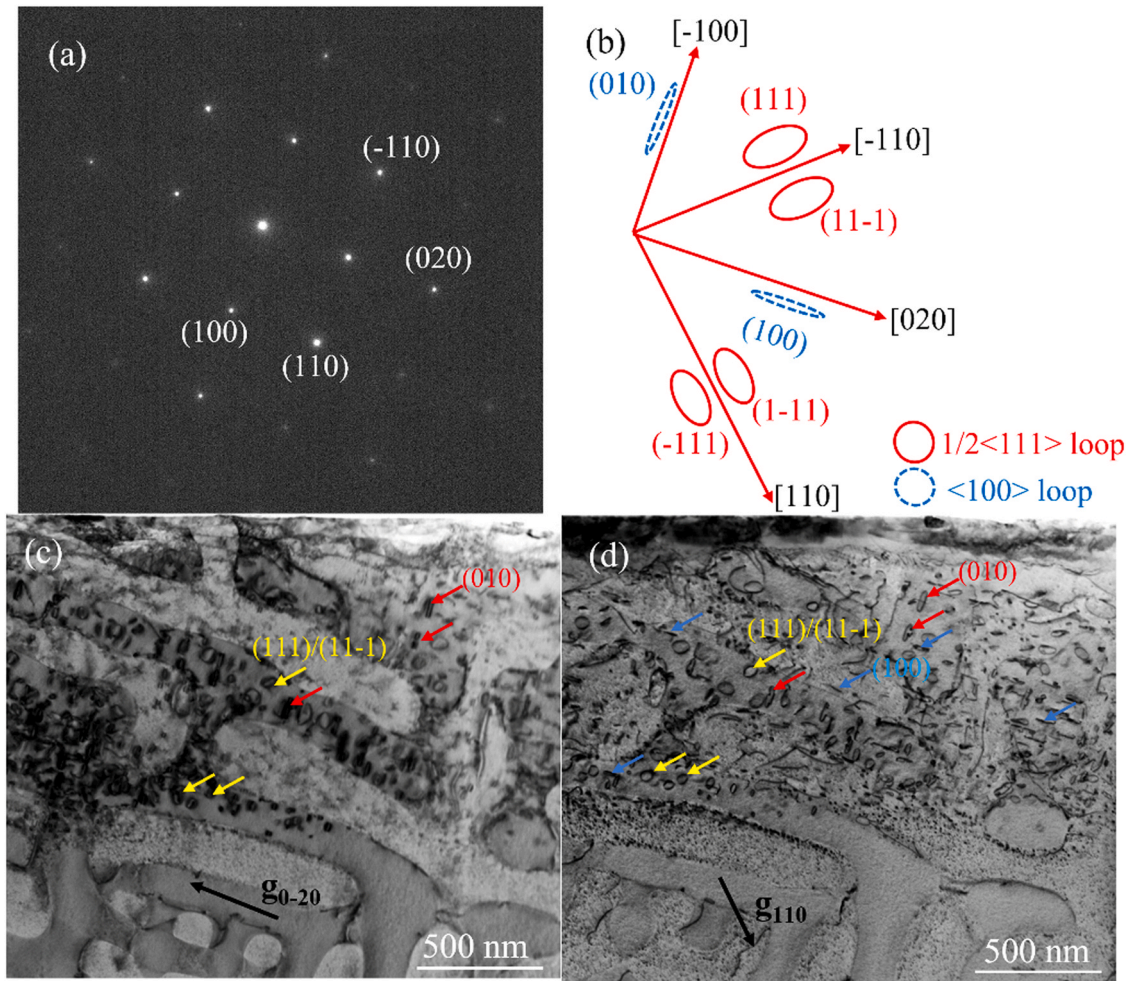
Fig. 1. (a) Diffraction pattern of Ti0 irradiated with 3 MeV Fe^{11+} ions to 4.55×10^{15} (1.4 dpa) ions/cm^2 under [001] zone axis. (b) Corresponding dislocation loops morphology map at on-zone condition. (c) and (d) are the corresponding bright-field images by using $\boldsymbol{g_{0\bar{2}0}}$ and $\boldsymbol{g_{110}}$ diffraction vectors near the zone axis, respectively.

Some studies have shown that the majority of dislocation loops in ferritic/martensitic steels are < 100 > dislocation loops when the irradiation temperature is higher than 350 °C [22,23]. In this study, the lower density of < 100 > compared to that of 1/2 < 111 > indicates that only part of 1/2 < 111 > dislocation loops are translated into < 100 > dislocation loops in the alloys after irradiation to 7 dpa at 500 °C, which further proving the great irradiation resistance of EHEA AlCrFeNi.

3.2. Distribution of dislocation loops in AlCrFeNi

The BF and weak-beam DF (WBDF, g/3 g) TEM micrographs were collected in order to identity and count the size and density of dislocation loops precisely. The microstructures of Ti0 irradiated with different irradiation doses were compared as shown in Fig. 2(a–d). Results indicated dislocation loops and defects clusters are the only

defect feature in the irradiation sample without voids at the two irradiation fluences. Previous studies [24,25] have confirmed that vacancies preferred to gather to form clusters or voids in conventional metallic materials when the irradiation temperature followed the relationship T = 0.23–0.35 T$_m$ and continue to grow until saturation when T > 0.35 T$_m$. However, voids were not visible even at the irradiation temperature of 500 °C in this work. Considering the melting temperature T$_m$ of Ti0 is 1438 °C, the irradiation temperature is approximately 0.35 T$_m$. The phenomenon may be attributed to the unique lattice distortion and sluggish diffusion effect of HEAs, further hindering the migration of vacancies, thereby suppressing the formation and growth of voids at elevated temperatures [26].

TEM analysis in Fig. 2(a) shows that the dislocation loops in the B2 phase were distributed at larger sizes with considerably lower density than those in the A2 phase, at the irradiation dose lower than 7 dpa. However, the density of dislocation loops in the B2 phase

Table 1
$\boldsymbol{g \cdot b}$ value and crystallographic information between dislocation-loop habit planes and (002) plane when imaged under [001] zone axis.

Habit plane	(200)	(020)	(002)	(111)	($\bar{1}$11)	(1$\bar{1}$1)	(11$\bar{1}$)
Burgers vector **b**	a[100]	a[010]	a[001]	a/2[111]	a/2[$\bar{1}$11]	a/2[1$\bar{1}$1]	a/2[11$\bar{1}$]
Project angle (θ)	90	90	0	54	54	54	54
cos (θ)	0	0	1	0.58	0.58	0.58	0.58
Direction of intersection line	[020]	[200]	n/a	[$\bar{1}$10]	[110]	[110]	[$\bar{1}$10]
$\boldsymbol{g_{0\bar{2}0} \cdot b}$	0	-2	0	-2	-2	2	-2
$\boldsymbol{g_{110} \cdot b}$	1	1	0	2	0	0	2

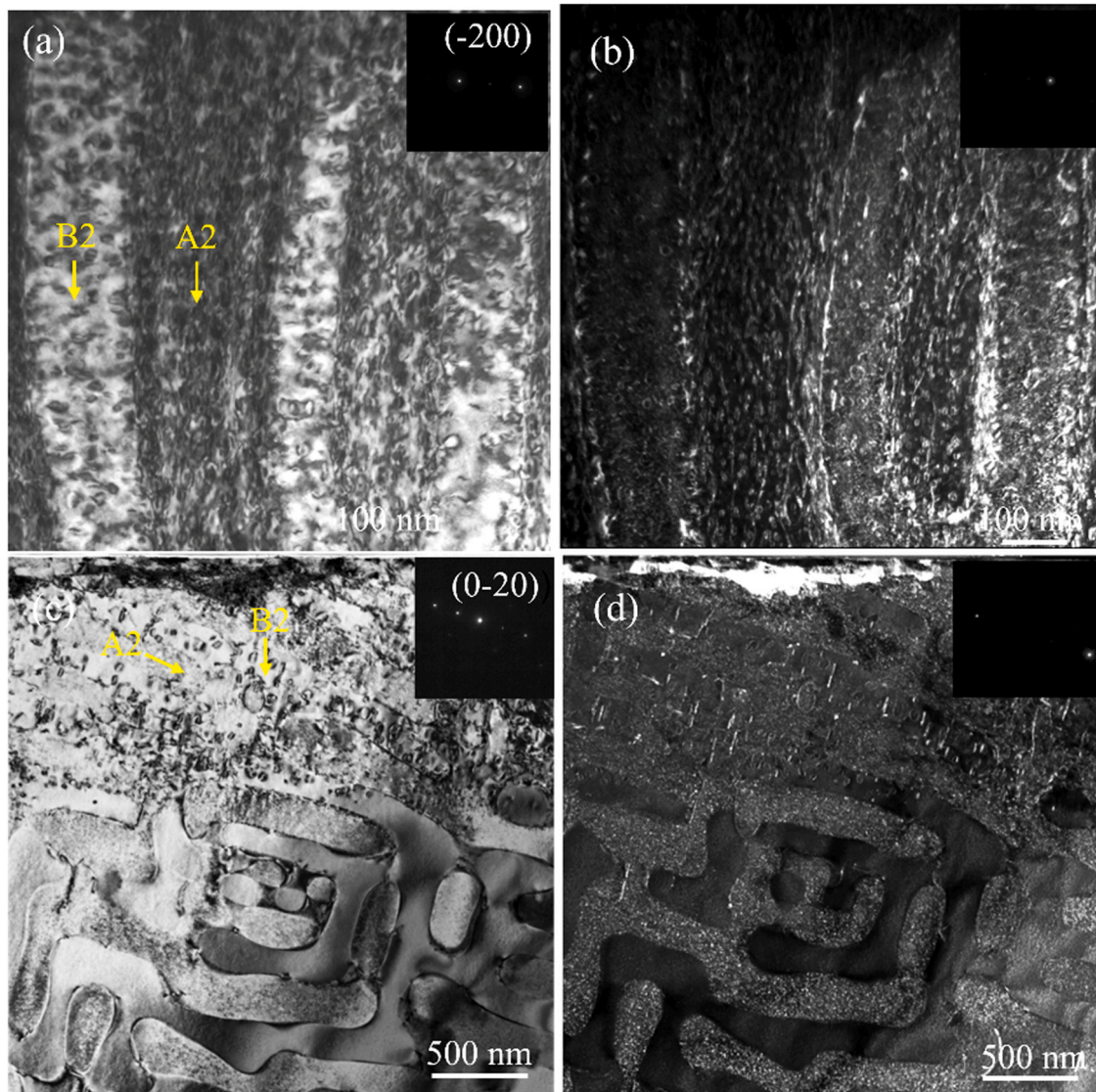**Fig. 2.** (a), (c) are the BF-TEM images of Ti0 irradiated by 3 MeV Fe^{11+} ions with dose of 9.1×10^{14} (1.4 dpa) and 4.55×10^{15} (7 dpa) ions/cm^2, respectively. (b) and (d) are the corresponding WBDF (g/3 g) images. (a) and (b) were obtained near the [011] zone axis with $\boldsymbol{g} = (\bar{2}00)$; (c) and (d) were obtained near the [001] zone axis with $\boldsymbol{g} = (0\bar{2}0)$.

is larger than that in the A2 phase at dose higher than 7 dpa, differing from that in Fig. 2(a). Fig. 3(a–d) shows the statistical results of dislocation loop size and number density. The loops distributed in the damage band were counted for statistics. The loop sizes were further determined by measuring the longest axis of the loops, which was summarized in Fig. 3(a) (c). The results showed that the loop sizes increased by increasing the irradiation dose, whereas the loop density became smaller. The size of dislocation loops in A2 and B2 phases irradiated with 1.4 dpa mainly layerd in the range of 6 –15 and 11 – 25 nm separately, with the corresponding number density of 1.16×10^{22} and 2.91×10^{21} /m^3, respectively. Moreover, the size of dislocation loops in A2 and B2 phases irradiated with 7 dpa was among the range of 16 – 30 and 36 – 50 nm, with the corresponding number densities of 1.32×10^{21} and 1.88×10^{21} /m^3, respectively.

3.3. Distribution of dislocation loops in AlCrFeNiTi$_{0.5}$ and AlCrFeNiTi

For Ti0.5 alloy, a representative BF-STEM image (Fig. 4(a)) shows that numerous spherical particles, which can be identified as defect clusters are distributed throughout the B2 matrix, consistent with previous results [13,25]. High density of large defect clusters and small-size dislocation loops which tend to form around the particles

were observed in the B2 phase. Compared to Ti0 alloy, numerous dislocation lines can be found in A2 and B2 phases in Ti0.5. The number and size of dislocation loops summarized in Fig. 5 indicated that dislocation loops in A2 and B2 phase of Ti0.5 are distributed at remarkably smaller sizes and much higher density than those in Ti0. Meanwhile, B2 exhibited smaller dislocation loops sizes and much higher density compared with A2 phase.

Fig. 4(b) shows the dislocation loops of Ti1 alloy, consisting of the A2 phase indicated by the SAED pattern. A TEM sample lamella without a phase boundary was prepared to confirm the effect of the phase boundary on defects distribution. The characterization results are summarized in Fig. 5. The width of the defect band in Ti1 is smaller than that in Ti0. Ti can be dissolved in the A2 phase to increase the lattice distortion, thus decreasing the width of the defect band [27], which can be evidenced by the results herein, suggesting the width of the defect band in Ti1 is smaller than that in Ti0. However, the size and density of dislocation loops in Ti1 are larger than those in Ti0, which can be attributed to significant lower grain boundaries. Phase boundaries effectively reduce defects through acting as sinks for absorbing vacancies and interstitials [6,7], so that density of dislocation loops in Ti0 are smaller than that of Ti1, as shown in Fig. 5.
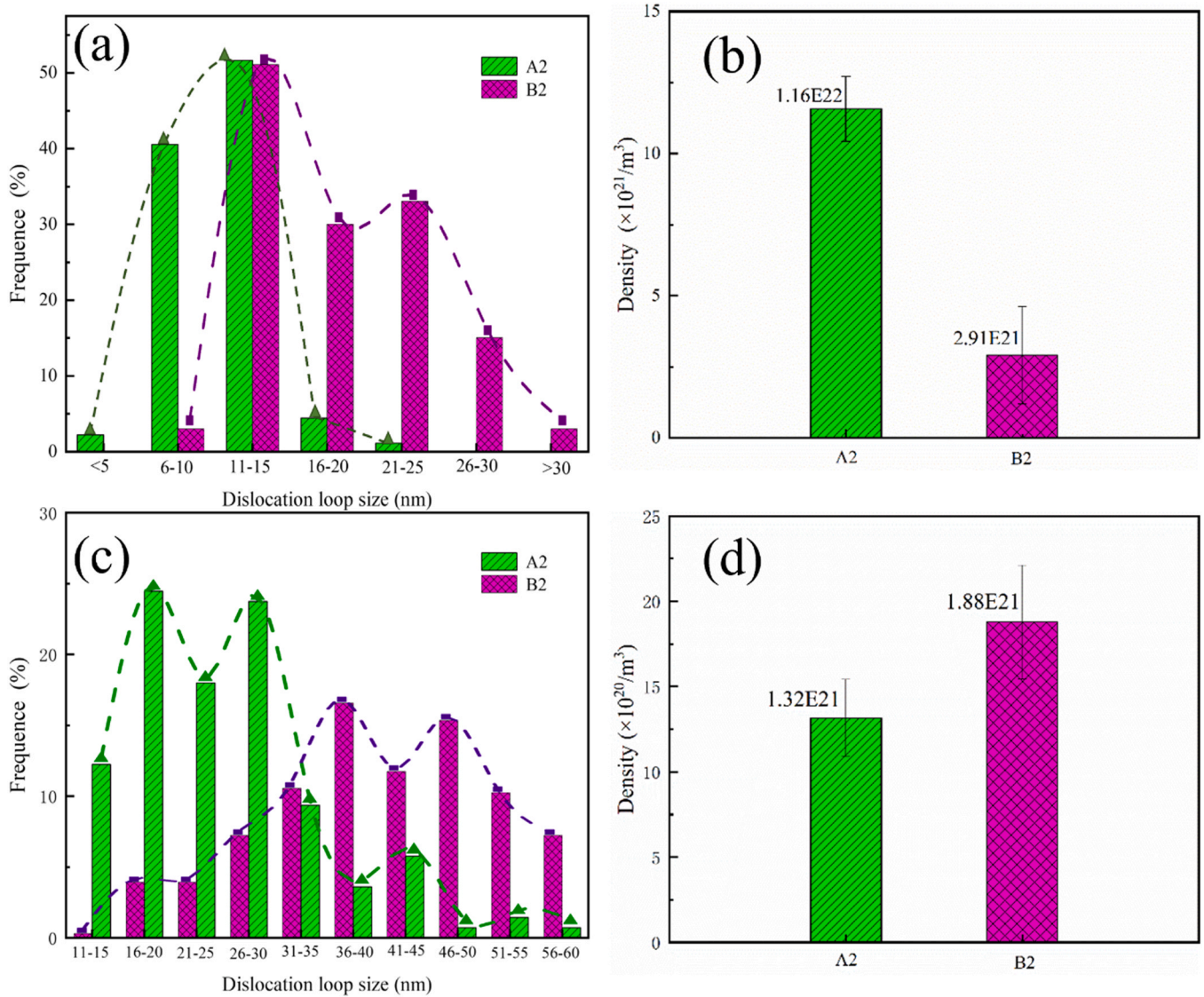
Fig. 3. Size distribution and density of dislocation loops in irradiated Ti0: (a), (b) irradiated with 3 MeV Fe^{11+} ions at 9.1×10^{14} (1.4 dpa) ions/cm^2; (c), (d) irradiated at 4.55×10^{15} (7 dpa) ions/cm^2. (a), (c) are the size distribution of dislocation loops in A2 and B2 phases; (b), (d) are the density of the A2 and B2 phases.

4. Discussion

According to the result in Fig. 3, AlCrFeNiTi$_x$ exhibited different radiation resistance in the A2/B2 phase. The kinetic mechanism of dislocation loops formation can be mainly divided into defects generation and migration, which is evidenced by the continuous absorption of migratable defects by interstitial atomic clusters and cavities leading to their own growth or contraction [28,29]. The vacancies formation energy of atoms in the A2/B2 phase was calculated via DFT method, and the point defect formation energies were 0.266, 0.73, 0.74, and 1.47 eV, respectively. Ni in the B2 phase demonstrated the lowest point defect formation energy, followed by Cr and Fe in A2 and Al in B2. Theoretically, B2 can generate vacancies more easily than A2, which is consistent with the fact that the density of dislocation loops in A2 is higher than B2 at 1.4 dpa. According to the dislocation loops size in Fig. 5, A2 is smaller than that in B2, whatever it is exposed to 1.4 dpa or 7 dpa. The obvious short-range disorder of A2 has strong effect on inhibiting the growth of dislocation loops, which makes the overall dislocation loops size smaller. The degree of lattice distortion of A2 and B2 can be concluded by the radial distribution function (RDF) in Fig. 6, and it is found that the lattice distortion of A2 is more obvious than that of

B2. The existence of local disordered phase will significantly reduce the diffusion rate of defects and further affect the growth of dislocation loops.

Based on the above study, the results indicated that the formation of dislocation loops was affected by local lattice distortion and energy landscape. Therefore, Ti in different types of atomic vacancy positions as well as interstitial positions was calculated by trapping energy, which is expressed as [30,31]:

$$E_{trap-x} = E_{A2/B2}(1Ti, V) - E_{A2/B2}(V) - E_{A2/B2}(Ti - interstitial) + E_{A2/B2}$$
(5)

where E_{trap-x} is the trapping energy when Ti is in the vacancy of atoms, x represents the atom species, $E_{A2/B2}(1Ti, V)$ is the system energy of Ti in lattice site, $E_{A2/B2}(V)$ is the system energy including vacancy of A2/B2 phase, $E_{A2/B2}(Ti - interstitial)$ is the lowest energy when Ti is in interstitial position, the energy of A2 and B2 are 13.37 eV and 3.95 eV, respectively. $E_{A2/B2}$ is the energy of A2/B2 system. Overall, $E_{trap-Al}$, $E_{trap-Ni}$, $E_{trap-Fe}$ and $E_{trap-Cr}$ are -6.47, -4.26, -3.73 and -3.42 eV, respectively. From the trapping energy results, it can be concluded that Al vacancy in B2 phase was easier to capture Ti atoms compared to A2, which was consistent with the experimental results of more Ti nanoparticles in B2 phase, further
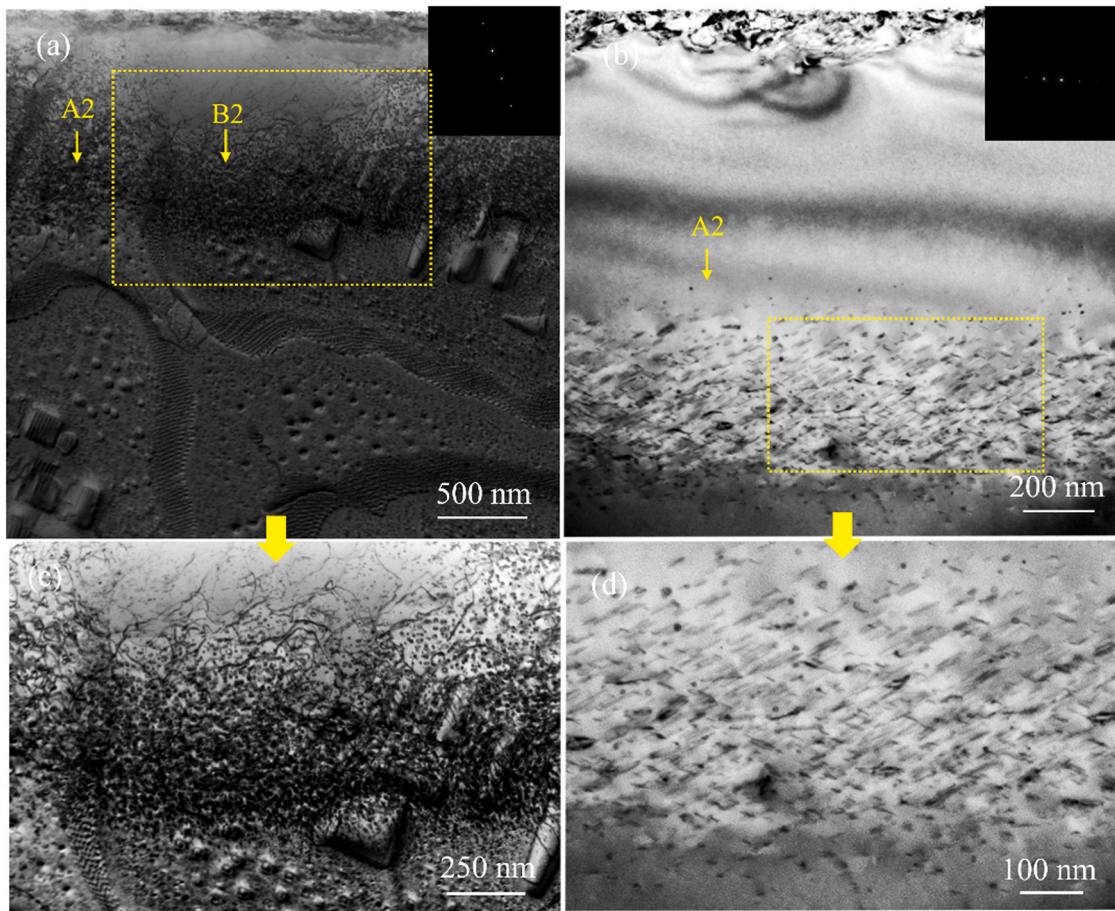
Fig. 4. (a) Defect band BF-STEM image at damage peak region of Ti0.5 irradiated at fluence to 4.55×10^{15} (7 dpa) ions/cm^2. (b) Defect band BF-TEM image at damage peak region of Ti1 irradiated at fluence to 4.55×10^{15} ions/cm^2. (a) was obtained near the [001] zone axis with $\boldsymbol{g} = (110)$; (b) was obtained near the [011] zone axis with $\boldsymbol{g} = (0\bar{1}1)$. (c) and (d) are the enlarged images of (a) and (b), respectively.
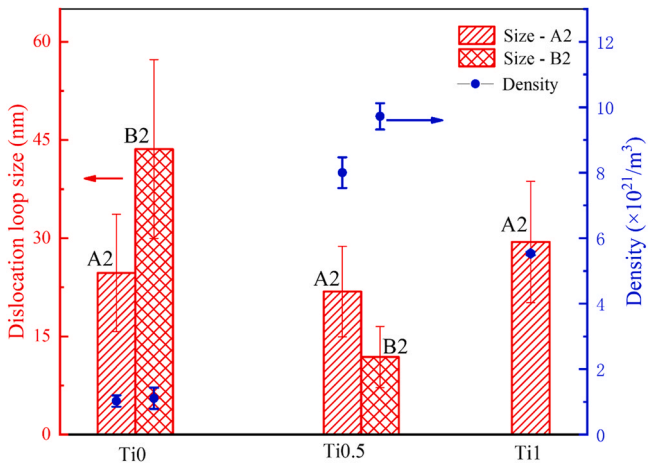

Fig. 5. Statistical results of the size and number densities of observed dislocation loops for the samples with different Ti contents irradiated at fluence to 4.55×10^{15} (7 dpa) ions/cm^2. All the results were obtained with $\boldsymbol{g} = (110)$.
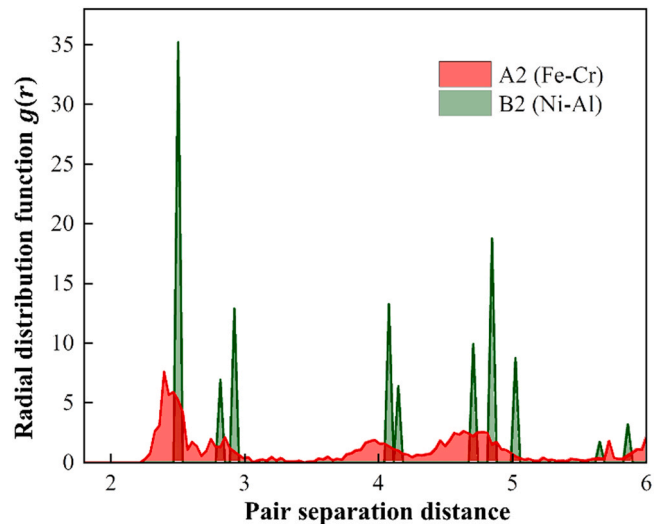

Fig. 6. The RDF diagram of A2 and B2 systems after relaxation.

evidenced by the ratio of Ti in A2 to B2 was about 2:3 in our previous research [14], which can be attributed to the synergetic effect of lower defect formation energy in B2 phase and higher interstitial energy in the disordered lattice of A2. Furthermore, the evolution of A2 and B2 systems under the working conditions (770 K) was analyzed by AIMD method with a time frame of 1 *ps*. The MSD results found that the average ionic mobility of B2 increased from

0.117×10^{-3} to 0.818×10^{-3} cm^2/s/V after Ti was added, which was higher than 0.696×10^{-3} cm^2/s/V of A2, indicating a large atomic displacement occurred in B2 phase, indicating the lattice distortion of B2 phase is significantly increased as shown in Fig. 7.

Overall, A2 phase showed stronger radiation resistance of dislocation loops formation under Ti0, which can effectively hinder the growth of dislocation loops. However, B2 dominated the trapping
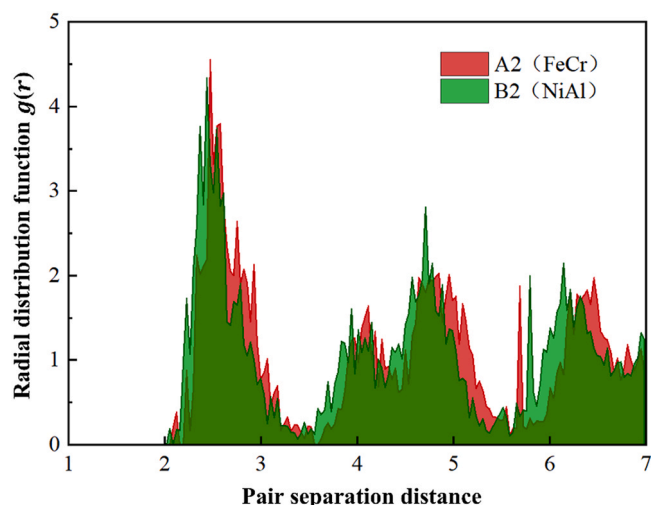
Fig. 7. The RDF diagram of A2 and B2 systems after Ti atom added.

ability of Ti atoms, which significantly enhanced the average ionic mobility from MSD results, and further caused lattice distortion of B2 with the increasing ratio of Ti. It can be inferred from the results that widely distributed Ti nanoparticles provided greater lattice distortion due to the high entropy effect, which will show a better ability to inhibit the migration of defects under the irradiation of 7 dpa. Although the effect of phase grain boundaries of Ti1 on the nano-scale was not directly observed, the calculation can still provide a theoretical explanation for the density and size changes of dislocation loops in A2.

5. Conclusion

In conclusion, three EHEAs AlCrFeNiTi$_x$ (x = 0, 0.5, 1) were irradiated with 3 MeV Fe ions under the highest fluence of 4.55×10^{15} ions/cm^2 at 500 °C, and the dislocation loops were characterized by TEM and STEM.

- Results show that the size of dislocation loops in the A2 phase was smaller than that in the B2 phase. Both < 100 > and 1/2 < 111 > dislocation loops were identified in Ti0 irradiated at a fluence of 4.55×10^{15} ions/cm^2 at 500 °C.
- Furthermore, small size and large density of dislocation loops formed in Ti0.5 especially in B2 phase.
- The DFT calculation results exhibited that B2 can capture more Ti atoms than A2, which can form bigger lattice distortion locally in B2. Combined with the experimental results, the widespread distribution of Ti nanoparticles in B2 has caused a high entropy effect that hinders the movement of defects, showing the relatively excellent radiation resistance than A2.

CRediT authorship contribution statement

Yibo Wang: Conceptualization, Methodology, Software, Validation, Formal analysis, Investigation, Data curation, Writing – original draft, Writing – review & editing. **Songyuan Li:** Conceptualization, Methodology, Software, Validation, Formal analysis, Investigation, Data curation, Writing – original draft, Writing – review & editing. **Feida Chen:** Conceptualization, Writing – original draft, Writing – review & editing, Funding acquisition. **Kun Yang:** Conceptualization, Writing – original draft, Writing – review & editing, Formal analysis, Funding acquisition. **Guojia Ge:** Investigation, Writing – original draft. **Xiaobin Tang:** Writing – original draft, Supervision, Project administration, Funding acquisition. **Minyu Fan:** Investigation. **Ping Huang:** Investigation.

Declaration of Competing Interest

The authors declare that they have no known competing financial interests or personal relationships that could have appeared to influence the work reported in this paper.

Appendix A. Supporting information

Supplementary data associated with this article can be found in the online version at doi:10.1016/j.jallcom.2023.170373.

References

[1] D.B. Miracle, O.N. Senkov, A critical review of high entropy alloys and related concepts, Acta Mater. 122 (2017) 448–511, https://doi.org/10.1016/j.actamat.2016.08.081

[2] E.P. George, W.A. Curtin, C.C. Tasan, High entropy alloys: a focused review of mechanical properties and deformation mechanisms, Acta Mater. 188 (2020) 435–474, https://doi.org/10.1016/j.actamat.2019.12.015

[3] M. Wang, et al., Lightweight, ultrastrong and high thermal-stable eutectic high-entropy alloys for elevated-temperature applications, Acta Mater. 248 (2023) 118806, https://doi.org/10.1016/j.actamat.2023.118806

[4] P. Shi, et al., Multistage work hardening assisted by multi-type twinning in ultrafine-grained heterostructural eutectic high-entropy alloys, Mater. Today 41 (2020) 62–71, https://doi.org/10.1016/j.mattod.2020.09.029

[5] M. Wang, et al., A novel bulk eutectic high-entropy alloy with outstanding as-cast specific yield strengths at elevated temperatures, Scr. Mater. 204 (2021) 114132, https://doi.org/10.1016/j.scriptamat.2021.114132

[6] W.Z. Han, M.J. Demkowicz, E.G. Fu, Y.Q. Wang, A. Misra, Effect of grain boundary character on sink efficiency, Acta Mater. 60 (18) (2012) 6341–6351, https://doi.org/10.1016/j.actamat.2012.08.009

[7] S.J. Zinkle, L.L. Snead, Designing radiation resistance in materials for fusion energy, Annu. Rev. Mater. Res. 44 (2014) 241–267, https://doi.org/10.1146/annurev-matsci-070813-113627

[8] J. Pang, et al., Atomic scale structure dominated FCC and B2 responses to He ion irradiation in eutectic high-entropy alloy AlCoCrFeNi$_{2.1}$, J. Mater. Sci. Technol. 129 (2022) 87–95, https://doi.org/10.1016/j.jmst.2022.04.023

[9] Y. Chen, et al., Heavy ion irradiation effects on CrFeMnNi and AlCrFeMnNi high entropy alloys, J. Nucl. Mater. 574 (2023) 154163, https://doi.org/10.1016/j.jnucmat.2022.154163

[10] B. Yao, D.J. Edwards, R.J. Kurtz, TEM characterization of dislocation loops in irradiated bcc Fe-based steels, J. Nucl. Mater. 434 (1–3) (2013) 402–410, https://doi.org/10.1016/j.jnucmat.2012.12.002

[11] X. Wang, W. Zhai, J.Y. Wang, B. Wei, Strength and ductility enhancement of high-entropy FeCoNi$_2$Al$_{0.9}$ alloy by ultrasonically refining eutectic structures, Scr. Mater. 225 (2023) 115154, https://doi.org/10.1016/j.scriptamat.2022.115154

[12] T. Shi, PH. Lei, X. Yan, et al., Current development of body-centered cubic high-entropy alloys for nuclear applications, Tungsten 3 (2021) 197–217 https://doi.org/10.1007/s42864-021-00086-6.

[13] M. Sadeghilaridjani, et al., Ion irradiation response and mechanical behavior of reduced activity high entropy alloy, J. Nucl. Mater. 529 (2020) 151955, https://doi.org/10.1016/j.jnucmat.2019.151955

[14] S. Li, et al., Effect of Ti on thE microstructure and mechanical properties of AlCrFeNiTix eutectic high-entropy alloys, J. Mater. Eng. Perform. 31 (10) (2022) 8294–8303, https://doi.org/10.1007/s11665-022-06825-1

[15] X. Chen, et al., Influences of Ti additions on the microstructure and tensile properties of AlCoCrFeNi$_{2.1}$ eutectic high entropy alloy, Intermetallics 128 (2021) 1–10, https://doi.org/10.1016/j.intermet.2020.107024

[16] L. Qiao, Aorigele, Z. Lai, J. Zhu, A promising new class of multi-component alloys with exceptional mechanical properties, J. Alloy. Compd. 847 (2020), https://doi.org/10.1016/j.jallcom.2020.155929

[17] G. Pu, et al., Outstanding radiation tolerance and mechanical behavior in ultra-fine nanocrystalline Al$_{1.5}$CoCrFeNi high entropy alloy films under He ion irradiation, Appl. Surf. Sci. 516 (2019) (2020), https://doi.org/10.1016/j.apsusc.2020.146129

[18] G. Kresse, J. Hafner, Ab initio molecular dynamics for liquid metals, Phys. Rev. B 47 (1) (1993) 558–561, https://doi.org/10.1103/PhysRevB.47.558

[19] G. Kresse, J. Furthmüller, Efficiency of ab-initio total energy calculations for metals and semiconductors using a plane-wave basis set, Comput. Mater. Sci. 6 (1) (1996) 15–50, https://doi.org/10.1016/0927-0256(96)00008-0

[20] V. Wang, N. Xu, J.C. Liu, G. Tang, W.T. Geng, VASPKIT: a user-friendly interface facilitating high-throughput computing and analysis using VASP code, Comput. Phys. Commun. 267 (2021) 108033, https://doi.org/10.1016/j.cpc.2021.108033

[21] B. Yao, D.J. Edwards, R.J. Kurtz, TEM characterization of dislocation loops in irradiated bcc Fe-based steels, J. Nucl. Mater. 434 (1–3) (2013) 402–410, https://doi.org/10.1016/j.jnucmat.2012.12.002

[22] F. Luo, et al., Damage behavior in helium-irradiated reduced-activation martensitic steels at elevated temperatures, J. Nucl. Mater. 455 (1–3) (2014) 339–342, https://doi.org/10.1016/j.jnucmat.2014.07.013

[23] X.G.R. zhouming, Liu Xinyi, Chen Zhe, Wang Hao, Li Yipeng, Evolution of dislocation loops in 30 keV He$^+$-irradiated W−0.5 % ZrC Alloys: In situ TEM observations and Molecular Dynamics simulations, Appl. Energy Mater. (2022) 2442–2451, https://doi.org/10.1021/acsaem.1c03915

[24] U. Theis, H. Wollenberger, Mobile interstitials produced by neutron irradiation in copper and aluminium, J. Nucl. Mater. 88 (1) (1980) 121–130, https://doi.org/10.1016/0022-3115(80)90392-X

[25] P. Ehrhart, R.S. Averback, Diffuse X-ray scattering studies of neutron- and electron-irradiated Ni, Cu and dilute alloys, Philos. Mag. A Phys. Condens. Matter Struct. Defects Mech. Prop. 60 (3) (1989) 283–306, https://doi.org/10.1080/01418618908213863

[26] N. Li, et al., Achieving a high-strength CoCrFeNiCu high-entropy alloy with an ultrafine-grained structure via friction stir processing, Acta Metall. Sin. (Engl. Lett. 33 (7) (2020) 947–956, https://doi.org/10.1007/s40195-020-01037-9

[27] Z.M. Jiao, et al., Superior mechanical properties of AlCoCrFeNiTix high-entropy alloys upon dynamic loading, J. Mater. Eng. Perform. 25 (2) (2016) 451–456, https://doi.org/10.1007/s11665-015-1869-3

[28] N.A.P.K. Kumar, C. Li, K.J. Leonard, H. Bei, S.J. Zinkle, Microstructural stability and mechanical behavior of FeNiMnCr high entropy alloy under ion irradiation, Acta Mater. 113 (2016) 230–244, https://doi.org/10.1016/j.actamat.2016.05.007

[29] C. Lu, et al., Radiation-induced segregation on defect clusters in single-phase concentrated solid-solution alloys, Acta Mater. 127 (2017) 98–107, https://doi.org/10.1016/j.actamat.2017.01.019

[30] Y.L. Liu, Y. Zhang, H.B. Zhou, G.H. Lu, F. Liu, G.N. Luo, Vacancy trapping mechanism for hydrogen bubble formation in metal, Phys. Rev. B - Condens. Matter Mater. Phys. 79 (17) (2009) 1–4, https://doi.org/10.1103/PhysRevB.79.172103

[31] C. Duan, et al., First-principles study on dissolution and diffusion properties of hydrogen in molybdenum, J. Nucl. Mater. 404 (2) (2010) 109–115, https://doi.org/10.1016/j.jnucmat.2010.06.029